Targeting RBM10 deficiency in lung adenocarcinoma

Feras E. Machour[1], Enas Abu-Zhayia[1], Joyce Kamar[2], Alma Sophia Barisaac[1]
Itamar Simon[2], Nabieh Ayoub*[1]

[1]Department of Biology, Technion - Israel Institute of Technology, Haifa 3200003, Israel.
[2]Department of Microbiology and Molecular Genetics, Institute of Medical Research Israel-Canada, Faculty of Medicine, The Hebrew University, Jerusalem, Israel

*Corresponding author: Prof. Nabieh Ayoub, Faculty of Biology
Technion - Israel Institute of Technology
Haifa 3200003, Israel.
Tel: +972-4-8294232 Fax: +972-4-8225153
Email: ayoubn@technion.ac.il

Abstract

Lung adenocarcinoma (LUAD) is a leading cause of cancer-related deaths worldwide[1,2]. The splicing factor RBM10 is commonly mutated in various cancer types and is strikingly one of the most mutated genes in LUAD (~9-25%)[3–7]. Most RBM10 cancer mutations are loss-of-function that correlate with increased tumorigenesis and poor survival[8–12], and limit the efficacy of targeted therapies in EGFR-mutated lung cancer[13]. Notably, exploiting RBM10 deficiency for targeted cancer therapy has not yet been explored, highlighting the urgency of identifying genetic vulnerabilities to RBM10 loss. Prompted by this, we performed a genome-wide CRISPR-Cas9 synthetic lethal (SL) screen in isogenic LUAD cell line harboring RBM10 cancer mutation and identified 262 high-scoring RBM10 SL genes, including Aurora A and WEE1 kinases. We show that pharmacological inhibition of WEE1 selectively sensitizes RBM10-deficient LUAD cells, including patient-derived cells harboring RBM10 cancer mutations, *in vitro* and in mouse xenograft model. Moreover, the sensitivity of RBM10-deficient cells to WEE1 inhibition is further exacerbated by combined treatment with Aurora kinase A inhibitor. Mechanistically, we demonstrate that the sensitivity to WEE1 inhibition is irrespective of RBM10 splicing activity, and potentiated by DNA damage accumulation, replication stress, and premature mitotic entry. Interestingly, we also reveal an unexpected role of RBM10 in promoting replication fork progression and stress response, at least in part, through its association with replication fork components. Collectively, our data identify DNA replication stress as an SL pathway with RBM10 loss, and provide a repertoire of targets that can be harnessed therapeutically to eradicate RBM10-deficient tumors.

Introduction

Lung cancer has the highest mortality rate among all types of cancer worldwide[1,2]. Non-small cell lung cancer (NSCLC) comprises 85% of all lung cancer cases and is subdivided into different subtypes including lung adenocarcinoma (LUAD) (40%)[14,15]. Most LUAD patients are diagnosed at advanced or metastatic stage, when treatment options are limited to surgery, chemotherapy, and few targeted therapies[15]. EGFR and KRAS are the most mutated oncogenes in LUAD amongst Asian (60%) and Caucasian (33%) cohorts, respectively[3,11]. Accordingly, several targeted therapies, including EGFR and KRAS inhibition, are currently used in the clinic for the treatment of advanced stages of LUAD harboring KRAS and EGFR mutations[16,17]. However, effective treatment of LUAD remains elusive due to the genetic diversity of the disease and the development of therapeutic resistance. Thus, there is a critical need for identifying new therapeutic targets for personalized treatment of LUAD. Interestingly, RNA-binding proteins are broadly dysregulated in human cancers including LUAD and play a key role in carcinogenesis and metastatic progression[18–26]. Therefore, alterations in RNA-binding proteins might provide excellent therapeutic targets for treating lung cancer. One very attractive and yet unexplored therapeutic target is the RNA-binding protein, RBM10.

RBM10 is mapped to the X chromosome[27], and its mutations cause TARP syndrome, an X-linked disorder that leads to pre-and postnatal lethality in affected males[28–34]. RBM10 is a key regulator of alternative splicing that mainly promotes exon skipping of its target genes[35–41]. Also, RBM10 impacts chromatin structure and chromosome segregation independently of its splicing activity[42–45]. Mounting evidence show that RBM10 acts as a tumor suppressor, as its depletion increases cell proliferation and enhances mouse xenograft tumor formation[9–11,38,41,46–49]. Concordantly, RBM10 overexpression suppresses LUAD tumor growth *in vivo*[11,50]. RBM10 exerts its tumor suppressive activity through various mechanisms[38,47,51]. For example, it was shown that RBM10 inhibits cell proliferation and tumor growth through alternative splicing regulation of NUMB and EIF4H genes[10,11,41]

RBM10 is the most mutated splicing factor in LUAD and is mutated in 9% of all LUAD cases[3]. Strikingly, this percentage rises to 21% in invasive subtypes of LUAD, and 25% in multiple primary LUAD[4,6]. Moreover, RBM10 mutation rate is higher than KRAS and TP53 mutations in early stages of LUAD in patients from Asian origin[5,7]. Most RBM10 mutations in LUAD correspond to loss-of-function and are associated with poor survival[8,12]. Notably, RBM10 mutations mostly co-occur with EGFR and KRAS mutations and were shown to reduce the efficiency of tyrosine kinase inhibitors (TKIs) in LUAD patients harboring EGFR

mutations[11,13]. Altogether, these findings highlight the urgency of therapeutic targeting of RBM10-deficiency in LUAD.

Herein, we performed a genome-wide CRISPR-Cas9 synthetic lethal (SL) screen to identify genetic vulnerabilities for eliminating RBM10-deficient LUAD cells. Our results revealed 262 RBM10 SL genes including Aurora A and WEE1 kinases. We demonstrated that pharmacological inhibition of WEE1 suppresses the growth of RBM10-deficient LUAD cells *in vitro* and in mouse xenograft model, and this effect was further exacerbated when combined with Aurora A inhibition. In addition, we identified replication stress and premature mitotic entry as the molecular basis underlying RBM10-WEE1 synthetic lethality. Moreover, we revealed a hitherto unrecognized role of RBM10 splicing factor in replication fork progression and replication stress response. Collectively, our work provides a preclinical basis for using WEE1 inhibitor as a single agent or in combination with Aurora A inhibition, as new therapeutic strategies for targeting RBM10-deficiency in LUAD.

Results

Genome-wide CRISPR-Cas9 screen reveals synthetic lethal partners of RBM10 in LUAD cells

Given that RBM10 is one of the most mutated genes in LUAD, we sought to identify genetic vulnerabilities to RBM10 loss. To achieve this, we conducted an unbiased genome-scale CRISPR-Cas9 SL screen in LUAD HCC827 cell line. HCC827 cells harbor a common oncogenic deletion in EGFR (E746-A750), and are a pertinent model to screen for genetic vulnerabilities to RBM10 loss since RBM10 and EGFR mutations often co-occur in LUAD, and RBM10 loss was shown to limit the response to common EGFR-targeted therapy[11,13]. Therefore, we sought to generate isogenic HCC827 cells stably expressing comparable levels of flag-Cas9 endonuclease and differ only in the status of RBM10. Toward this end, we designed a gRNA targeting RBM10 exon 2 to introduce a frameshift mutation V176Rfs*, that exhibits a complete absence of RBM10 protein, while constitutively expressing Cas9 protein (HCC827-Cas9$^{RBM10\text{-}KO}$) (Fig. 1a and Supplementary Fig. 1a,b). Interestingly, the introduced mutation closely resembles a previously characterized LUAD cancer mutation E177* that abrogates RBM10 splicing activity and leads to RBM10 protein loss[12]. Notably, HCC827-Cas9$^{RBM10\text{-}KO}$ cells exhibit an increase in exon inclusion of RBM10 splicing targets NUMB and EIF4H, phenocopying the defective splicing phenotype of RBM10-deficient LUAD[11,41](Fig. 1b and Supplementary Fig. 1c).

Next, we conducted a genome-scale CRISPR-Cas9 SL screen in the isogenic HCC827-Cas9^{WT} and HCC827-Cas9$^{RBM10\text{-}KO}$ using the TKOv1 sgRNA library, which contains 91,320 sgRNAs targeting 17,232 protein-coding genes[52]. Cells were collected at 0, 15, and 30 days following TKOv1 library transduction and subjected to next-generation sequencing to measure sgRNA abundance (Supplementary Fig. 1d). Bayesian Analysis of Gene Essentiality (BAGEL) machine-learning algorithm[53] was applied to search for genes that are essential in HCC827-Cas9$^{RBM10\text{-}KO}$ cells at T15 and T30, but nonessential in the parental HCC827-Cas9^{WT} cells. Using these criteria, we identified 262 RBM10 synthetic lethal candidate genes (Fig. 1c and Supplementary Table 1). Gene-set enrichment analysis revealed significant enrichment of several pathways including RNA processing, intra-S and G2/M cell cycle checkpoints, and DNA replication (Fig. 1d). To functionally validate the screen results, we conditionally knocked-down 5 genes annotated to various enriched pathways (SF3B1, WAPAL, WEE1, AURKA, PEX10), followed by clonogenic survival assay. Results showed that depletion of these genes selectively inhibited the proliferation of HCC827-Cas9$^{RBM10\text{-}KO}$ cells, with negligible effect on parental cells, confirming successful identification of bona-fide RBM10 SL genes (Fig. 1e and Supplementary Fig. 1e). Interestingly, several RBM10 SL genes, such as WAPAL, MUS81, WEE1, and DNA2, have known functions in DNA replication stress response and replication fork protection, thus suggesting DNA replication stress as a synthetic lethal pathway with RBM10 deficiency in LUAD (Fig. 1f).

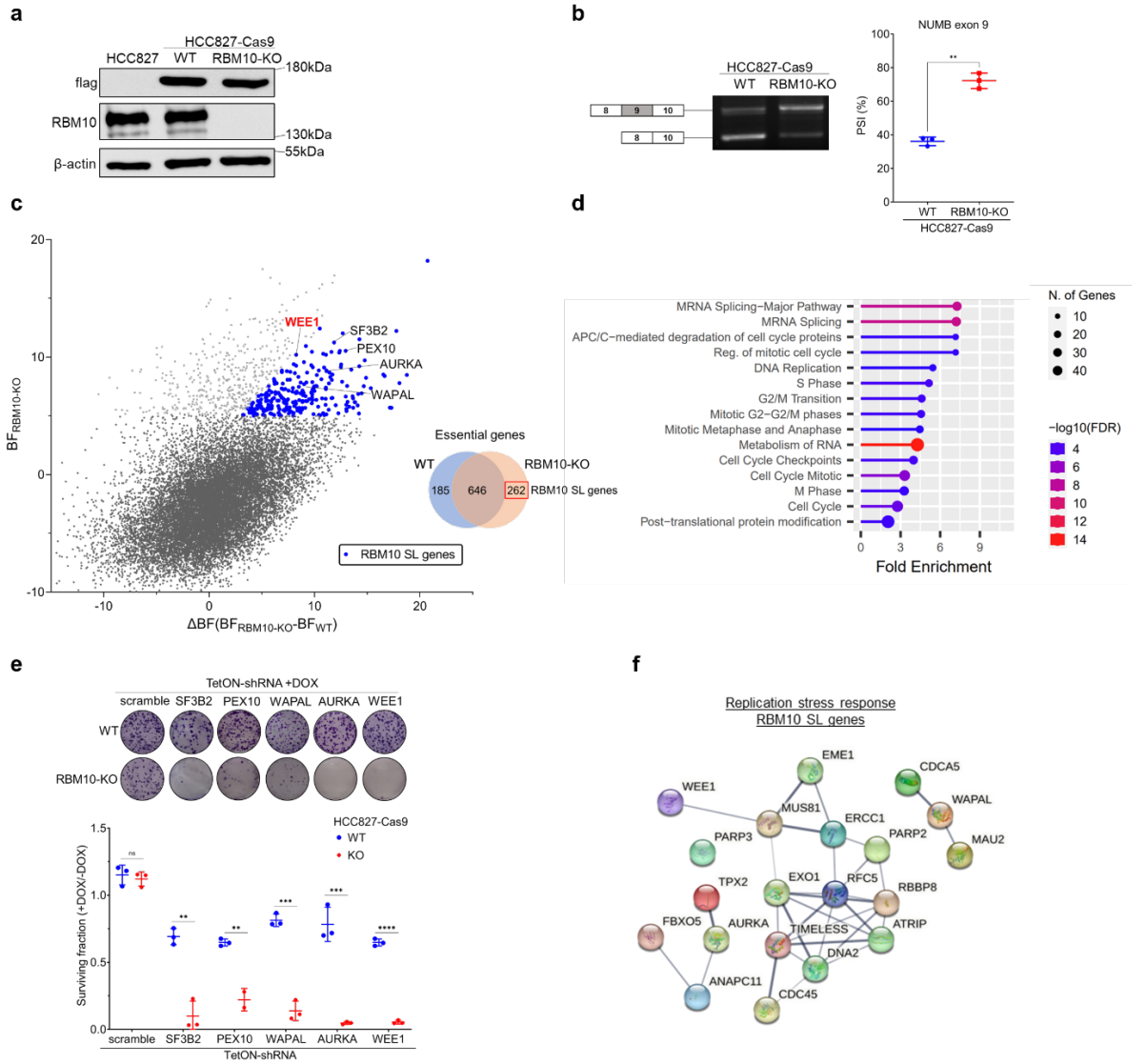

Figure 1: Genome-wide CRISPR-Cas9 screen reveals synthetic lethal partners of RBM10 in LUAD cells. (a) Immunoblot analysis for RBM10 and flag-Cas9 protein expression in isogenic RBM10-deficient HCC827 cells constitutively expressing flag-Cas9. β-actin is used as a loading control. The positions of molecular weight markers are indicated to the right. **(b)** RT-PCR analysis of NUMB exon 9 alternative splicing in parental (WT) and HCC827-Cas9$^{RBM10\text{-}KO}$ cells. RNA was isolated from the indicated cell lines and analyzed by RT-PCR using primers flanking NUMB exons 8-10. Left: Representative agarose gel image showing amplification of two NUMB variants that differ in exon 9 inclusion. Right: Precent-spliced-in (PSI) quantification of NUMB exon 9 inclusion. Data are presented as mean ± s.d. (n=3). ***$P< 0.001$. **(c)** Results of CRISPR-Cas9 SL screen in WT and HCC827-Cas9$^{RBM10\text{-}KO}$ cells performed in triplicates. Left: Gene essentiality, expressed as Bayes Factor (BF), in RBM10-KO cells is plotted against the BF difference (ΔBF) between RBM10-KO and WT cells. RBM10 SL genes are shown in blue. Right: Venn diagram showing the intersection of essential genes in WT and RBM10-KO cells. **(d)** Gene ontology analysis of RBM10 SL genes identified in the CRISPR-Cas9 SL screen. **(e)** Clonogenic survival of WT and HCC827-Cas9$^{RBM10\text{-}KO}$ cells transduced with inducible vector expressing either scramble shRNA or shRNA targeting the indicated genes upon the addition of doxycycline (DOX). Top: Representative images of crystal violet staining of the indicated cell lines treated with DOX. Bottom: Quantification of clonogenic survival in DOX-treated cells normalized to untreated cells. Data are presented as

mean ± s.d. (n=3). ***P<0.01;****P<0.001;*****P<0.0001.* **(f)** STRING interaction network of RBM10 SL genes involved in replication stress response. The thickness of the connecting line indicates interaction confidence.

WEE1 kinase inhibition selectively sensitizes RBM10-deficient LUAD cells

Herein, we focused on WEE1 kinase, since it is a high scoring RBM10 SL gene and is involved in several RBM10 SL pathways, such as intra-S and G2/M cell cycle checkpoints[54,55]. Moreover, WEE1 has a small molecule inhibitor, MK1775 (AZD1775), which is currently in several phase II clinical trials for treatment of advanced solid tumors (ClinicalTrials.gov), highlighting the clinical potential for targeting RBM10-deficient LUAD[56–58]. To test whether the observed RBM10-WEE1 synthetic lethality (Fig. 1e) is dependent on WEE1 kinase activity, we pharmacologically inhibited WEE1 using MK1775 in parental HCC827-Cas9^{WT} and HCC827-Cas9$^{RBM10\text{-}KO}$ cells. Short and long-term survival assays revealed that HCC827-Cas9$^{RBM10\text{-}KO}$ cells exhibit pronounced sensitivity to MK1775 treatment compared to parental cells (Fig. 2a,b and Supplementary Fig 2a). The hypersensitivity of RBM10-deficient cells to MK1775 was also observed in a second RBM10-KO clone (KO2) isolated from HCC827-Cas9 cells (Figure 2A-B), and in RBM10-KO (KO3) cells derived from naïve HCC827 cells that don't stably express Cas9, suggesting that WEE1-RBM10 synthetic lethality is not due to a clonal effect or cytotoxicity caused by stable expression of Cas9 endonuclease (Supplementary Fig. 2b,c). Since RBM10 modulates the splicing of hundreds of genes, we sought to test whether RBM10 splicing activity underlies RBM10-WEE1 synthetic lethality. To do so, we generated a point mutation in the RRM domain of RBM10 (V354E) that was previously shown to hinder its alternative splicing function[10,12,41]. Next, we tested the sensitivity to MK1775 in RBM10-deficient cells complemented with a vector expressing either flag-RBM10-WT or flag-RBM10-V354E. Results showed that both RBM10-WT and RBM10-V354E expression suppressed the sensitivity to MK1775 to a similar extent, suggesting that RBM10-WEE1 synthetic lethality is independent of RBM10 splicing activity (Fig. 2c).

Since TP53 mutations often co-occur with RBM10 mutations in LUAD[59], we generated RBM10 knockout cell line in p53-deficient LUAD cells NCI-H1299 (H1299$^{RBM10\text{-}KO}$) (Supplementary Fig. 2d,e). Similar to p53-proficient HCC827, our results showed that H1299$^{RBM10\text{-}KO}$ cells are hypersensitive to MK1775 compared to control cells (Fig. 2d,e). To increase the therapeutic potential of our observations, we tested RBM10-WEE1 synthetic lethality in two RBM10-deficient patient-derived cell lines, NCI-H1944 (containing KRAS^{G13D} mutation) and NCI-H1975 (containing EGFR$^{L858R/T790M}$ mutation) harboring p.A683Rfs*10

and p.G905Afs*7 truncating RBM10 mutations, respectively. Towards this, NCI-H1944 and NCI-H1975 cells were transduced with flag-RBM10 expression vectors (Supplementary Fig. 2f,g) and treated with MK1775 followed by cell viability assays. Results showed that RBM10 expression rescues the sensitivity of RBM10-deficient cell lines to MK1775, suggesting that RBM10 loss occurring during LUAD tumorigenesis potentiates the sensitivity to WEE1 inhibition (Fig. 2f,g). Altogether, our results recapitulate RBM10-WEE1 synthetic lethality observed in our CRISPR-Cas9 SL screen and demonstrate that WEE1 inhibition selectively sensitizes RBM10-deficient LUAD tumor cells from different origins and independently of common co-occurring mutations such as EGFR, KRAS and TP53, highlighting the clinical relevance of targeting RBM10 loss in LUAD using MK1775.

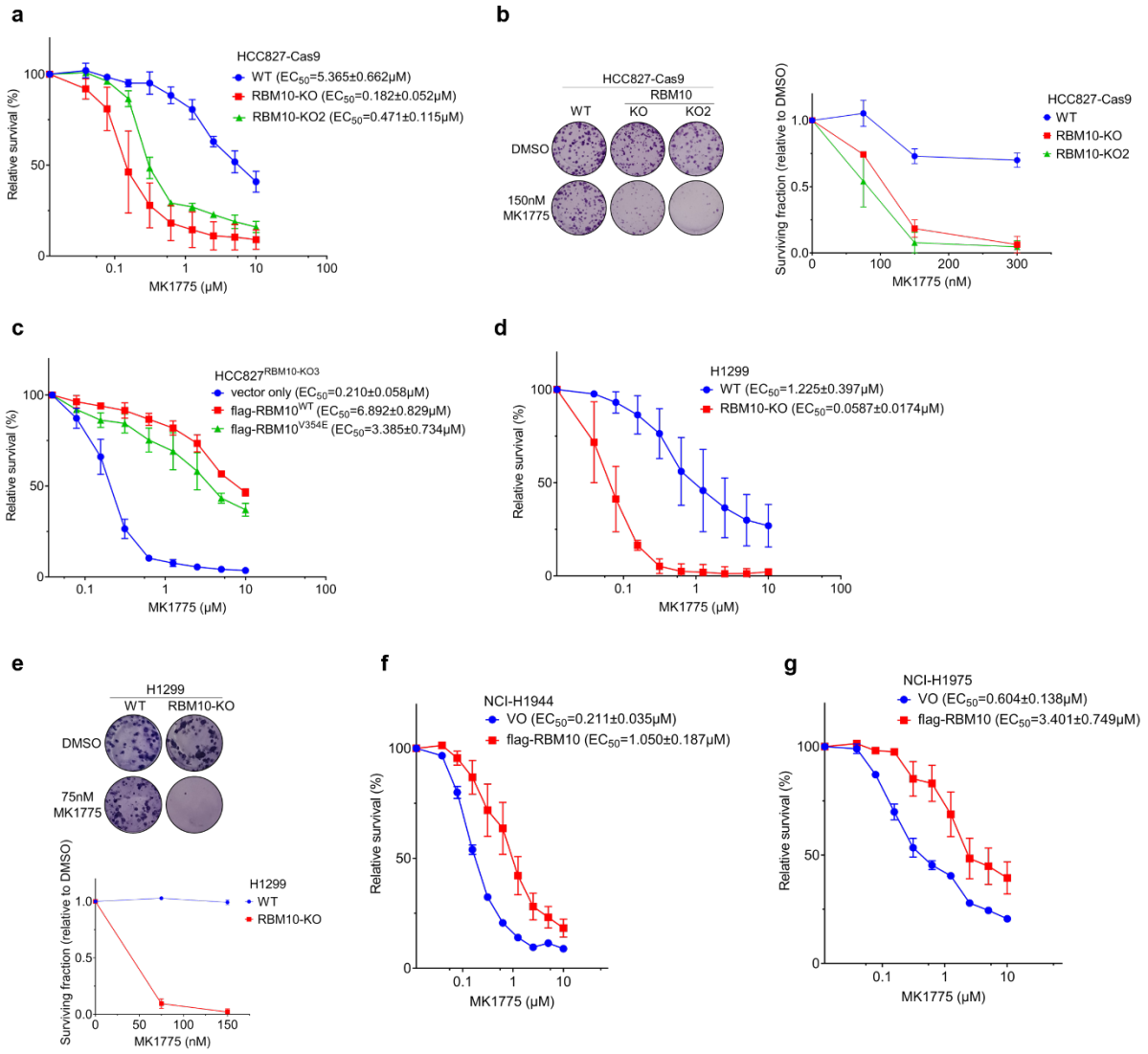

Figure 2: WEE1 kinase inhibition selectively sensitizes RBM10-deficient LUAD cells. (a) Short-term cell viability assay and EC_{50} determination in WT and two RBM10-KO clones (KO

and KO2) of HCC827-Cas9 cells treated with increasing concentrations of MK1775. Data are presented as mean ± s.d. (n=3). **(b)** Clonogenic survival of WT and two RBM10-KO clones treated with the indicated concentrations of MK1775. Left, representative images of plates stained with crystal violet. Right, quantification of clonogenic survival. Data are presented as mean ± s.d. (n=3). **(c)** As in (a), except of using HCC827$^{RBM10\text{-}KO3}$ cells expressing flag-RBM10-WT, flag-RBM10-V354E, or vector only. (**d**) As in (a), except of using H1299^{WT} and H1299$^{RBM10\text{-}KO}$ cells. **(e)** Clonogenic survival of H1299^{WT} and H1299$^{RBM10\text{-}KO}$ cells treated with the indicated concentrations of MK1775. Top, representative images of plates stained with crystal violet. Bottom, quantification of clonogenic survival. Data are presented as mean ± s.d. (n=3). **(f,g)** As in (a), except of using NCI-H1944 (f) or NCI-H1975 (g) cells expressing either flag-RBM10-WT or vector only.

DNA damage and premature mitotic entry underpin RBM10-WEE1 synthetic lethality

We sought to decipher the molecular basis underlying the hypersensitivity of RBM10-deficient cells to WEE1 inhibition. We showed that H1299$^{RBM10\text{-}KO}$ cells treated with increasing concentrations of MK1775 exhibit elevated levels of phosphorylated histone H2A.X (γH2AX), suggesting that DNA damage accumulation upon WEE1 inhibition is exacerbated in RBM10-deficient cells (Fig. 3a). Likewise, higher levels of stalled forks and replication stress markers including phosphorylated RPA32 on positions 4 and 8 (pRPA32-S4/S8), RPA32 on position 33 (pRPA32-S33), and CHK1 on position 345 (pCHK1-S345) were observed in MK1775-treated H1299$^{RBM10\text{-}KO}$ cells compared to control cells (Fig. 3b and Supplementary Fig 3a,b). Also, native BrdU staining revealed an increase in single-stranded DNA (ssDNA) accumulation in H1299$^{RBM10\text{-}KO}$ cells upon MK1775 treatment, indicating that MK1775-induced replication stress is aggravated in RBM10-deficient cells (Fig. 3c,d). In addition, MK1775-treated H1299$^{RBM10\text{-}KO}$ cells exhibit high levels of micronucleation, extensive nuclear γH2AX staining and apoptosis (Fig. 3e,g). Altogether, our data imply that replication stress-associated genomic instabilities underlie the hypersensitivity of RBM10-deficient cells to WEE1 inhibition.

Next, we sought to determine the effect of WEE1 inhibition on cell cycle progression in RBM10-deficient cells. Towards this, parental and H1299$^{RBM10\text{-}KO}$ cells were co-stained for pH3(Ser10), a marker of early mitosis, and EdU as a marker for S-phase following MK1775 treatment. Remarkably, unlike parental cells, a significant fraction (~45%) of MK1775-treated H1299$^{RBM10\text{-}KO}$ cells were co-stained with EdU and pH3(Ser10), suggesting that WEE1 inhibition leads to premature mitotic entry in RBM10-deficient cells (Fig. 3h,i). Similar results were also obtained in parental and HCC827$^{RBM10\text{-}KO}$ cells (Fig. 3j). Altogether, we concluded that the sensitivity of RBM10-deficient cells to MK1775 is mediated by increased replication stress and premature mitotic entry leading to mitotic catastrophe and cell death.

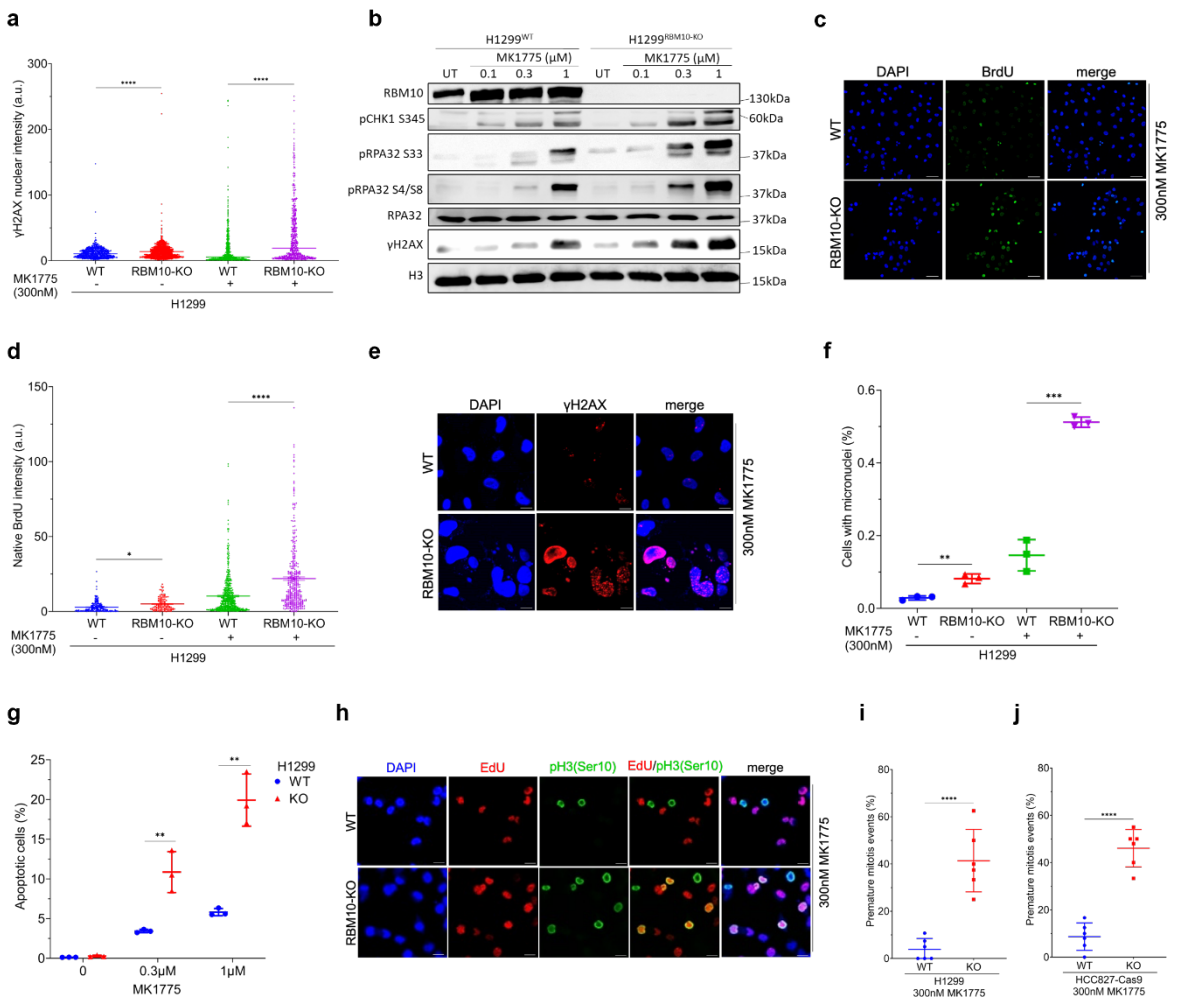

Figure 3: DNA damage and premature mitotic entry underpin RBM10-WEE1 synthetic lethality. (a) Quantification of γH2AX staining in H1299^{WT} and H1299$^{RBM10\text{-}KO}$ cells treated with 300nM MK1775 for 24 hr. Data are presented as mean nuclear intensity ± SEM (n>590 cells) and representative of 3 independent experiments. Statistical significance was determined by Mann-Whitney test. ****$P<0.0001$. **(b)** Immunoblot analysis of DNA damage and replication stress markers in H1299^{WT} and H1299$^{RBM10\text{-}KO}$ cells after MK1775 treatment. Cells were either left untreated (UT) or treated with the indicated concentrations of MK1775 for 24 hr followed by immunoblot analysis using the indicated antibodies. Histone H3 is used as a loading control. The positions of molecular weight markers are indicated to the right. **(c,d)** Analysis of ssDNA levels using native BrdU staining in H1299^{WT} and H1299$^{RBM10\text{-}KO}$ cells treated with 300nM MK1775 for 24 hr. (c) Representative immunofluorescence microscopy image for native BrdU staining. DAPI is used to stain nuclei. Scale bar, 50μm. (d) Quantification of native BrdU staining. Data are presented as mean nuclear intensity ± SEM (n>100 cells for untreated cells, n>300 for MK1775-treated cells) and representative of 3 independent experiments. Statistical significance was determined by Mann-Whitney test. ****$P<0.0001$. **(e)** Representative immunofluorescence microscopy images of γH2AX and DAPI staining in H1299^{WT} and H1299$^{RBM10\text{-}KO}$ cells treated with 300nM MK1775 for 24 hr. Scale bar, 10μm. **(f)** Quantification of micronuclei in H1299^{WT} and H1299$^{RBM10\text{-}KO}$ cells treated with 300nM MK1775 for 24 hr. Data are presented as the average percentage of cells with micronuclei ± SEM (n=3). Statistical significance was determined by unpaired t-test. ****$P<0.0001$. **(g)** Quantification of apoptosis in H1299^{WT} and H1299$^{RBM10\text{-}KO}$ cells treated

with the indicated concentrations of MK1775 for 24 hr. Cells were stained with Annexin V and propidium iodide and analyzed by FACS. Percentage of apoptotic cells was determined by %Annexin V–positive cells and data are presented as mean ± s.d. (n=3). Statistical significance was determined by unpaired t-test. ***P< 0.01*. **(h)** Representative immunofluorescence microscopy images showing premature mitotic entry in $H1299^{WT}$ and $H1299^{RBM10\text{-}KO}$ cells treated with MK1775. EdU incorporation and pH3(Ser10) were used to determine DNA synthesis and mitotic entry, respectively. DAPI is used to stain nuclei. Scale bar, 20µm. **(i,j)** Quantification of premature mitotic entry events in parental (WT) and $H1299^{RBM10\text{-}KO}$ (i) and $HCC827^{RBM10\text{-}KO}$ (j) cells. Premature mitosis events were calculated as the percentage of EdU-positive cells from the pH3(Ser10)-positive (mitotic) cells and presented as mean ± s.d. (n=6). Statistical significance was determined by unpaired t-test. ****P< 0.0001*.

RBM10 promotes replication fork progression and stress response

The following lines of evidence prompted us to investigate the involvement of RBM10 in replication fork progression. First, a genome-wide siRNA screen identified RBM10 as a candidate replication stress response gene[60]. Second, RBM10 was shown to interact with several proteins involved in DNA replication and repair in fission yeast[45]. Third, RBM10 CRISPR-Cas9 SL screen revealed an enrichment of genes involved in DNA replication and cell cycle checkpoints (Fig. 1d). Fourth, RBM10-deficient cells display an increase in replication stress response upon MK1775 treatment (Fig. 3). Consequently, we sought to determine the impact of RBM10 loss on replication fork progression using DNA fiber analysis. Results showed that RBM10 loss leads to significant replication fork slowdown, suggesting that RBM10 is required for proper fork progression (Fig. 4a and Supplementary Fig. 4). Interestingly, replication fork slowdown upon RBM10 loss is accompanied by an increase in the levels of pRPA32-S33 and γH2AX, likely due to accumulation of stalled replication forks and endogenous DNA damage (Fig. 4b-d). Since WEE1 inhibition in RBM10-deficient cells leads to excessive replication stress, we investigated the effect of MK1775 treatment on replication fork progression. Results showed that WEE1 inhibition exacerbates the decrease in replication fork rate in RBM10-deficient cells compared to parental cells (Fig. 4e). These findings strongly suggest that replication stress underpins, at least partly, RBM10-WEE1 synthetic lethality.

Next, we investigated the effect of RBM10 loss on the recovery from hydroxyurea (HU) induced replication stress. Results showed that RBM10-deficient cells display a significant increase in replication stress and damage markers after release from HU, indicative of defective replication fork recovery during replication stress (Fig. 4f). Corollary to this, RBM10-deficient cells are markedly more sensitive than RBM10-proficient cells to increasing HU concentrations

(Fig. 4g). Collectively, our results demonstrate that RBM10 fosters efficient DNA replication fork progression and fork recovery during replication stress.

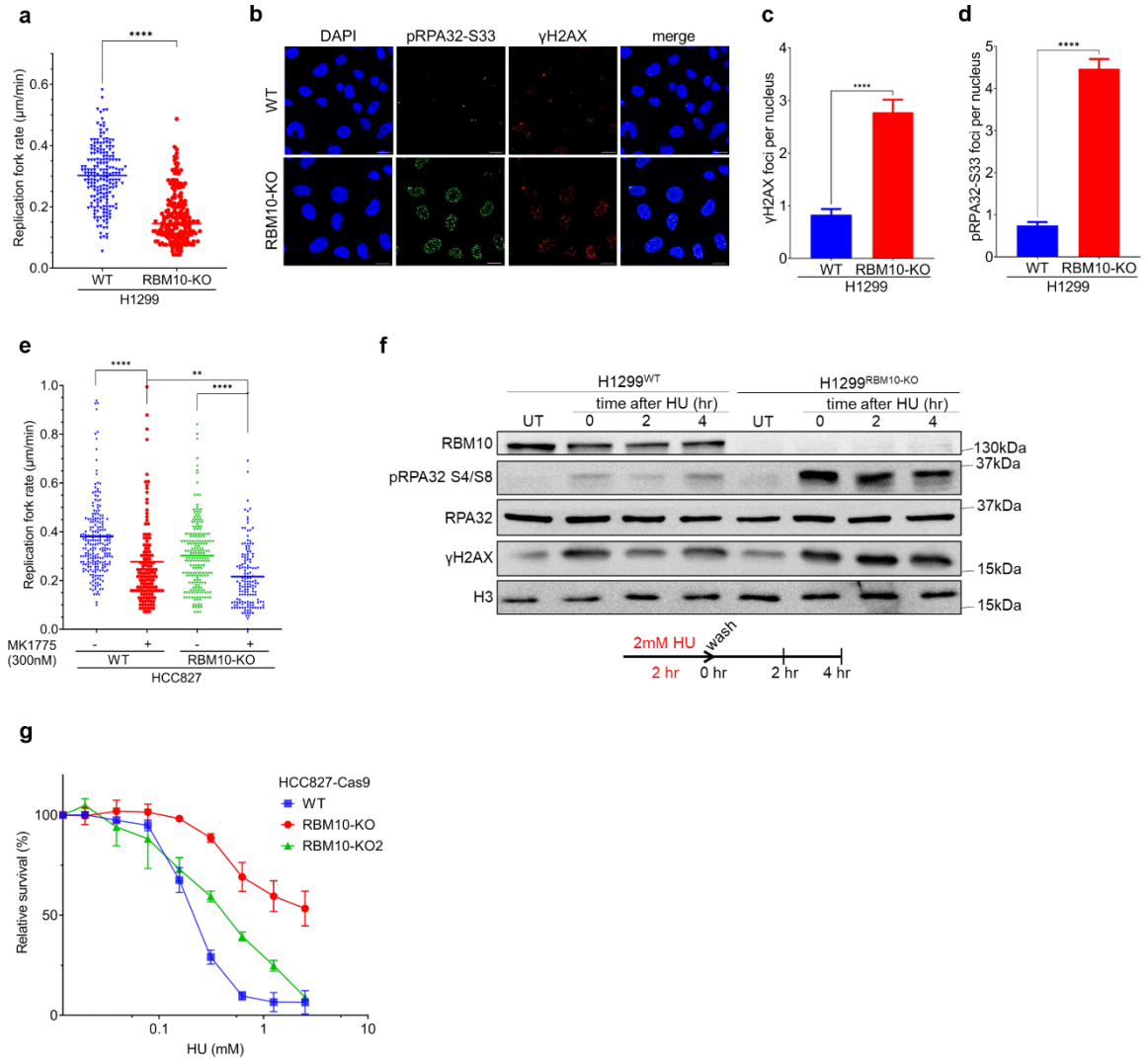

Figure 4: RBM10 promotes DNA replication fork progression and replication stress response. (a) Replication fork speed measurement using DNA combing assay in H1299^{WT} (n=194) and H1299$^{RBM10\text{-}KO}$ (n=197) cells. Black bars represent mean value. Statistical significance was determined by Mann-Whitney test. ****$P<0.0001$. **(b)** Representative immunofluorescence microscopy images of pRPA32-S33 and γH2AX foci in H1299^{WT} and H1299$^{RBM10\text{-}KO}$ cells. DAPI is used to stain nuclei. Scale bar, 20µm. **(c,d)** Quantification of γH2AX (c) and pRPA32-S33 (d) foci in H1299^{WT} and H1299$^{RBM10\text{-}KO}$ cells. Data are presented as mean foci number per nucleus ± SEM (n>200 cells) and representative of 3 independent experiments. Statistical significance was determined by Mann-Whitney test. ****$P<0.0001$. **(e)** DNA combing assay in HCC827-Cas9$^{RBM10\text{-}WT}$ and HCC827-Cas9$^{RBM10\text{-}KO}$ treated with MK1775. Replication fork speed (n>150) was measured in untreated cells and cells treated with 300nM MK1775 for 24 hr. Black bars represent mean value. Statistical significance was determined by Mann-Whitney test. **$P<0.01$;****$P<0.0001$. **(f)** H1299^{WT} and H1299$^{RBM10\text{-}KO}$ cells were treated with 2mM hydroxyurea (HU) for 2 hr and subjected to immunoblot analysis at the indicated times after release from HU. Histone H3 is used as a loading control.

UT=untreated. The positions of molecular weight markers are indicated to the right. **(g)** Short-term cell viability assay in parental (WT) and RBM10-KO HCC827-Cas9 cells treated with increasing concentrations of HU. Data are presented as mean ± s.d. (n=3).

RBM10 is associated with replication fork components

To gain molecular insights into the involvement of RBM10 in replication fork progression, we first determined its localization on chromatin. Biochemical fractionation revealed that RBM10 is enriched at the chromatin-bound fraction (Fig. 5a), supporting the notion that RBM10 has a direct role in regulating replication fork progression. To further substantiate this, we sought to map RBM10 interactome in unchallenged cells and following replication stress induced by WEE1 inhibition. Towards this, untreated and MK1775-treated cells expressing RBM10 fused to EGFP were subjected to GFP-trap followed by mass spectrometry (MS) analysis. Results revealed 410 RBM10-interacting proteins annotated to several pathways, most notably the spliceosome, consistent with RBM10 function in alternative splicing, as well as DNA replication. (Fig. 5b,c and Supplementary Table 2). Intriguingly, we revealed that RBM10 interacts with replication fork components and proteins involved in replication stress response, such as the MCM2-7 complex, PCNA, RAD51, and PARP1. Moreover, the interactions between RBM10 and these proteins were significantly higher following MK1775 treatment, further substantiating RBM10 direct role in replication stress (Fig. 5d).

Next, we validated the authenticity of RBM10 interactome and showed that RBM10 interacts with PARP1, RAD51 and PCNA (Fig. 5e). In addition, RBM10 interaction with PARP1 and RAD51 was enhanced following MK1775 treatment, consistent with our MS analysis. To further substantiate RBM10 interaction with replication forks, first we confirmed the interaction between endogenous RBM10 and PCNA in LUAD cells (Fig. 5f). Second, we tested whether RBM10 is associated with replication forks in cells using proximity ligation assay (PLA). Results showed that RBM10 is in close proximity to PCNA (Fig. 5g). Moreover, PLA combined with EdU click chemistry revealed that RBM10 is associated with EdU-labelled nascent DNA, marking sites of active DNA replication (Fig. 5h). Collectively, our data provide firm evidence that RBM10 interacts with replication forks under native conditions.

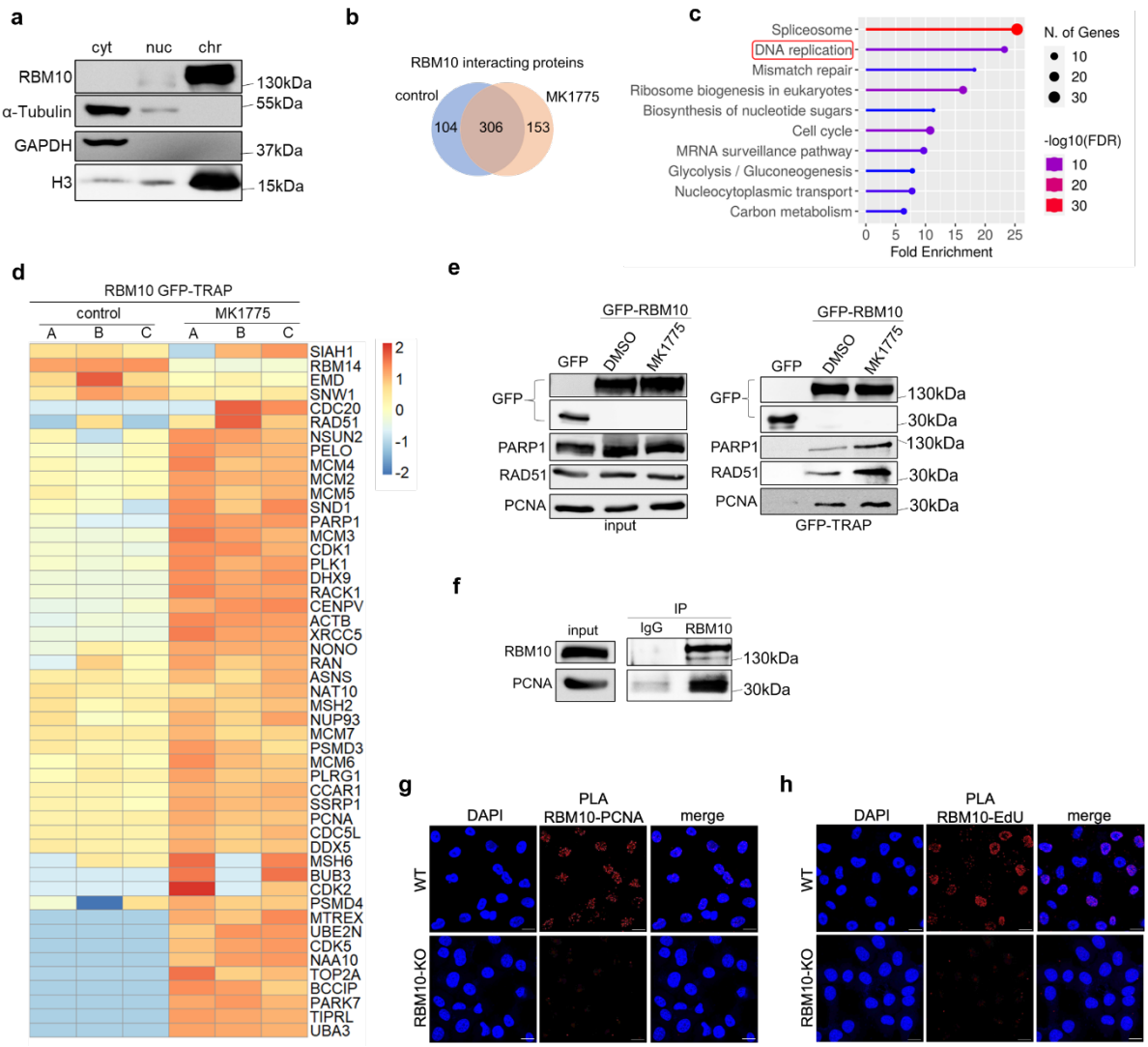

Figure 5: RBM10 is a DNA replication fork-associated protein. (a) Biochemical fractionation of HCC827 cells into cytosolic (cyt), nuclear-soluble (nuc), and chromatin-bound (chr) fractions followed by immunoblotting with the indicated antibodies. The positions of molecular weight markers are indicated to the right. **(b)** Venn diagram shows the intersection between RBM10-interacting proteins in untreated cells and cells treated with 300nM MK1775 for 4 hr. HEK-293T cells expressing two main RBM10 isoforms fused to EGFP were subjected to GFP-trap followed by mass spectrometry to identify RBM10 interactome before and after MK1775 treatment. **(c)** Gene ontology analysis of RBM10 interactome in unchallenged cells as identified by GFP-trap followed by mass spectrometry analysis. **(d)** Heatmap summarizing RBM10-interacting proteins involved in cell cycle regulation, DNA damage response, and replication stress before and after MK1775 treatment. Colors represent relative protein intensity of RBM10-interacting proteins in untreated cells and cells treated with 300nM MK1775 for 4 hr across 3 replicates as identified by GFP-trap followed mass spectrometry. **(e)** HEK293T cells expressing EGFP-RBM10 or EGFP only were treated either with DMSO or 300nM MK1775 for 4 hr and subjected to GFP-trap followed by immunoblot analysis using the indicated antibodies. The positions of molecular weight markers are indicated to the right. **(f)** Immunoprecipitation of endogenous RBM10 in H1299 cells. Whole-cell lysates from H1299 cells were subjected to immunoprecipitation using RBM10 antibody or IgG and subjected to immunoblot analysis with the indicated antibodies. The positions of molecular weight markers are indicated to the right. **(g,h)** Representative immunofluorescence

microscopy images of RBM10:PCNA (g) and RBM10:EdU-biotin (h) proximity ligation assay (PLA) foci in H1299^{WT} and H1299$^{RBM10\text{-}KO}$ cells. Scale bar, 20μm.

MK1775 inhibits the growth of RBM10-deficient LUAD tumors *in vivo*

Given that the WEE1 inhibitor MK1775 is currently undergoing phase II clinical trials for treating several tumor types[61], we sought to test the therapeutic potential of WEE1 inhibition against RBM10-deficient LUAD cells *in vivo*. Our results showed that MK1775 treatment prominently reduced the size of xenograft tumors derived from HCC827$^{RBM10\text{-}KO}$ and H1299$^{RBM10\text{-}KO}$ cells, but not their parental counterparts (Fig. 6a,b and Supplementary Fig. 5a,b). Consistent with the observed γH2A.X phenotype *in vitro*, RBM10-deficient tumors exhibit increased levels of DNA damage in MK1775-treated mice. (Fig. 6c,d and Supplementary Fig. 5c). Collectively, these findings strongly suggest that RBM10 loss leads to increased sensitivity to WEE1 inhibition *in vivo*, independently of EGFR or TP53 status. To further substantiate the clinical relevance of targeting RBM10-deficient LUAD, we tested the anti-tumor effect of MK1775 against tumor xenografts derived from patient-derived LUAD cells, NCI-H1944 and NCI-H1975, harboring naturally occurring RBM10 cancer mutations. Results showed that WEE1 inhibition leads to remarkable tumor growth inhibition in RBM10-deficient NCI-H1975 and NCI-H1944 compared to RBM10-proficient cells (Fig. 6e). Altogether, our results demonstrate the therapeutic efficacy of MK1775 as a single-agent in eradicating LUAD tumors harboring RBM10 deleterious cancer mutations.

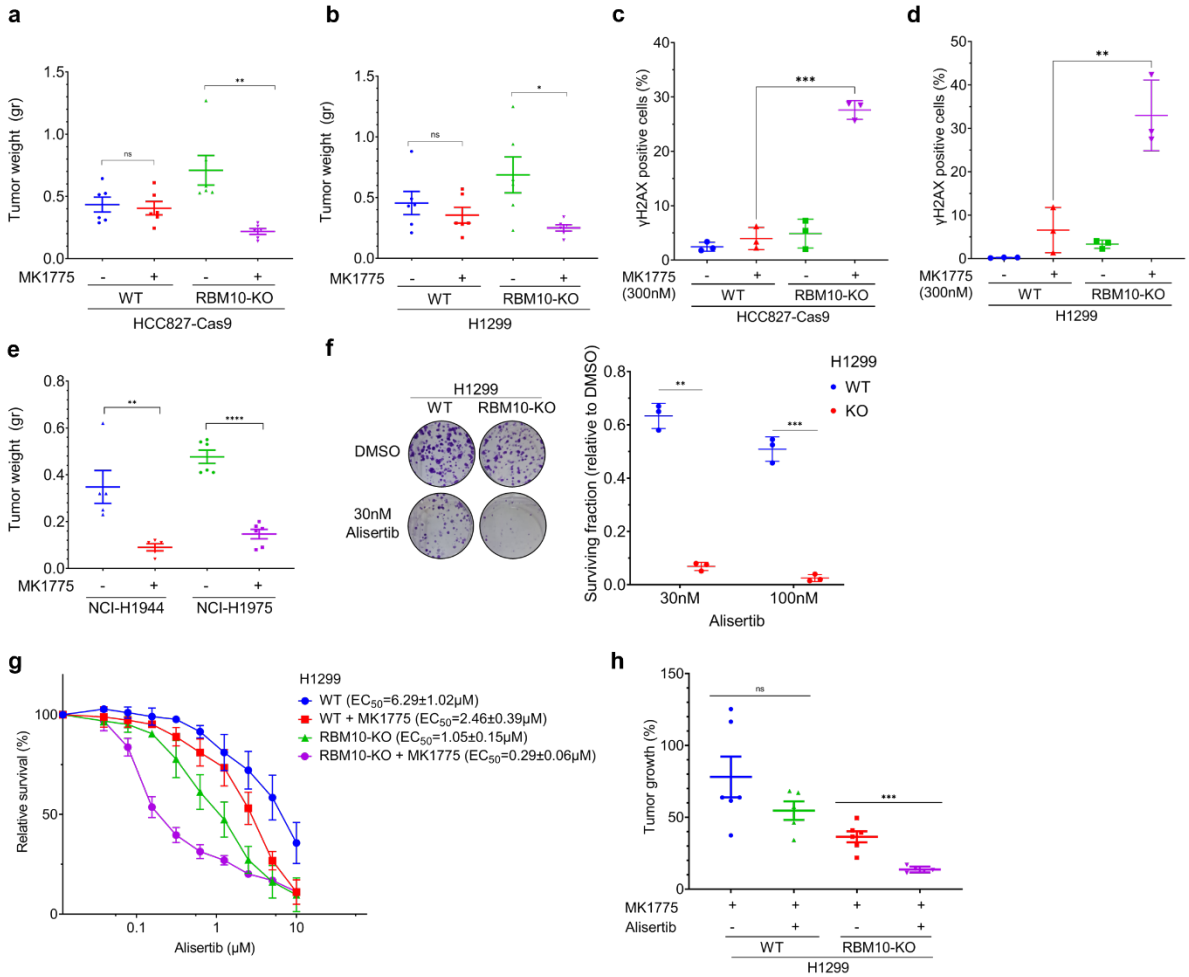

Figure 6: Alisertib enhances the anti-tumor activity of MK1775 against RBM10-deficient LUAD *in vivo*. (a,b) Tumor weight of parental (WT) and HCC827-Cas9$^{RBM10\text{-}KO}$ (a) and H1299$^{RBM10\text{-}KO}$ (b) xenografts treated with either MK1775 or vehicle. MK1775 was administered once daily at 40mg/kg for 15 days. Results are shown as mean tumor weight ± SEM (n=6). Statistical significance was determined by unpaired t-test. *$P<0.05$;**$P<0.01$. **(c,d)** Quantification of γH2AX immunostaining in xenograft tumor sections from parental and HCC827-Cas9$^{RBM10\text{-}KO}$ (c) and H1299$^{RBM10\text{-}KO}$ (d) tumors treated with either MK1775 or vehicle. Data are presented as the average percentage γH2AX positive cells ± SEM of 3 different tumor sections for each group. Statistical significance was determined by unpaired t-test. **$P<0.01$;***$P<0.001$. **(e)** Tumor weight of NCI-H1944 and NCI-H1975 xenografts treated with either MK1775 or vehicle. MK1775 was administered once daily at 40mg/kg for 15 days. Results are shown as mean tumor weight ± SEM (n=5 for NCI-H1944, n=6 for NCI-H1975). Statistical significance was determined by unpaired t-test. **$P<0.01$;****$P<0.00001$. **(f)** Clonogenic survival of H1299^{WT} and H1299$^{RBM10\text{-}KO}$ cells treated with the indicated concentrations of alisertib. Left, representative images of plates stained with crystal violet. Right, quantification of clonogenic survival. Data are presented as mean ± s.d. (n=3). **(g)** Short-term cell viability assay and EC_{50} determination in H1299^{WT} and H1299$^{RBM10\text{-}KO}$ cells treated with increasing concentrations of alisertib with or without treatment with 300nM MK1775. Data are presented as mean ± s.d. (n=3). **(h)** Tumor growth inhibition in H1299^{WT} and H1299$^{RBM10\text{-}KO}$ xenografts treated with MK1775 alone, MK1775 and alisertib combination, or vehicle. MK1775 alone or MK1775 and alisertib combination were administered once daily at 30mg/kg for 15 days. Results are shown as percentage tumor growth inhibition relative to

vehicle ± SEM (n=6 for MK1775 alone and vehicle, n=5 for MK1775 + alisertib combination). Statistical significance was determined by unpaired t-test. ***$P<0.001$.

Aurora kinase A inhibition exacerbates the anti-tumor activity of WEE1 inhibition in RBM10-deficient LUAD

Given that both WEE1 and Aurora A (AURKA) scored highly in RBM10 SL screen and both kinases are targeted by small molecule inhibitors undergoing clinical trials, we tested the efficacy of the combined Aurora A and WEE1 inhibition on the growth of RBM10-deficient LUAD. First, we observed that the Aurora A inhibitor, alisertib, had a profound effect on the clonogenic survival of RBM10 KO cells, concurrent with the CRISPR SL screen results (Fig. 6f and Supplementary Fig. 6d). Moreover, while alisertib alone led to a significant reduction in RBM10-deficient cell viability, combined MK1775 and alisertib treatment further exacerbated cell toxicity (Fig. 6g). Prompted by this, we tested the effect of the combined MK1775 and alisertib treatment on the growth of RBM10-deficient xenograft tumors. Results showed that the combined treatment leads to a profound and significant reduction in RBM10-deficient tumor size that is greater than the reduction upon MK1775 treatment alone (Fig. 6h). Therefore, we concluded that Aurora kinase A inhibition might be a viable therapeutic strategy to enhance the anti-tumor activity of WEE1 inhibition in RBM10-deficient LUAD tumors.

Discussion

Herein, we identified 262 RBM10 SL genes, such as WEE1 and Aurora A kinases, which can be therapeutically exploited for eradicating RBM10-deficient LUAD tumors. Indeed, pharmacological inhibition of WEE1 using MK1775 markedly reduces RBM10-deficient cell proliferation and tumor growth. Given that MK1775 is currently in phase II clinical trials for the treatment of several types of tumors, we propose that it can be also used against RBM10-deficient LUAD with immediate clinical applicability. Interestingly, the sensitivity of RBM10-deficient cells to WEE1 inhibition is further exacerbated by the combined treatment with alisertib, an Aurora Kinase A inhibitor. This is in line with a previous study showing that alisertib and MK1775 display a synergic anti-tumor effect in p53-deficient squamous cell carcinoma of the head and neck[62]. Together, these observations provide a basis for testing this combination for clinical treatment of RBM10-deficient LUAD patients, thus increasing therapeutic benefits and minimizing the risk for developing resistance.

Unexpectedly, RBM10 interactome analysis revealed that it interacts with various replication fork components that are required for proper replication fork progression, as well as recovery from replication stress. In addition, we confirmed that RBM10 physically interacts with PCNA

and is associated with active DNA replication forks *in vivo*. Also, RBM10 depletion leads to replication fork slowdown, which is accompanied by an increase in replication fork stalling and DNA damage. Moreover, RBM10-deficient cells are more vulnerable to HU-induced replication stress. Collectively, these findings describe a hitherto unknown role of RBM10 splicing factor in regulating replication fork progression and stress response. Our data are in line with a genome-wide siRNA screen that identified RNA processing factors, including RBM10, as replication stress response genes[60]. Moreover, previous studies showed that RBM10 is associated with human pre-replication complex[63]and interacts with several proteins involved in DNA replication and repair in fission yeast[45]. In this regard, it would be of interest to determine whether other RNA splicing and processing factors are also implicated in DNA replication.

Why RBM10 depletion leads to replication stress remains currently unknown. Since we observed that RBM10 is localized at active replication forks (Fig. 5h), we assume that it might serve as a platform for recruiting replication fork factors to ensure proper fork progression and recovery from stress. Our interactome data support this assumption, as RBM10 interacts with known replication stress mediators and this interaction is further enhanced upon MK1775 treatment (Fig. 5d). Alternatively, even though expression of splicing-deficient RBM10 rescues the sensitivity to WEE1 inhibition (Fig. 2c), we cannot exclude the possibility that RBM10 may regulate the splicing or expression of genes involved in regulating replication fork progression.

We demonstrated that RBM10-WEE1 synthetic lethality is mediated, at least in part, by increased replication stress leading to premature mitotic entry and cell death. Interestingly, our data suggest that RBM10-WEE1 synthetic lethality is independent of RBM10 splicing activity, as expression of RBM10 splicing mutant suppressed the sensitivity of RBM10-deficient cells to WEE1 inhibition. This finding supports the notion that the sensitivity of RBM10-deficient cells to WEE1 inhibition is dependent on the emerging role of RBM10 in DNA replication. Our data are therefore in agreement with previous studies showing synergistic interaction between WEE1 inhibition and replication stress-inducing agents[64–67].

Unbiased genome-wide CRISPR-Cas9 SL screens revolutionized the discovery of novel SL interactions that can be exploited for developing new cancer therapies[68,69]. Our CRISPR-Cas9 knockout screen revealed 262 RBM10 SL genes involved in various cellular pathways, such as RNA splicing and cell cycle. These genetic interactions advance our understanding of the

physiological functions of RBM10 and provide a repertoire of novel targets that can be harnessed to formulate new strategies for targeting RBM10-deficiency. Interestingly, RBM10 is frequently mutated in various human cancers such as endometrial (8%) and urothelial (5%) carcinomas[59]. Therefore, our findings might be of clinical interest to other types of human cancer harboring RBM10 mutations.

Acknowledgments

We thank Avigail Yampolsky and Yarin Attar for helping in validating the RBM10 CRISPR-Cas9 screen results, Dvir Aran for his help in analyzing RBM10 mutations in cancer, Yossi Shiloh and Yehuda Assaraf for their insightful comments on the project. We also thank Nadav Sharon, Assaf Bester, and Juan Valcárcel for generously sharing reagents and plasmids. We thank Janette Zavin for histological processing. We thank our lab members for critical reading of the manuscript. Research in the Ayoub lab is supported by grants from the Israel Science Foundation (2511/19) and Israel Cancer Research Fund (22-110-PG). Research in the Simon lab is supported by grants from the Israel Science Foundation (1283/21) and the Binational Science Foundation (2019688 and 2021085). F.E.M. and E.R.A. are supported by Clore fellowship. A.B. is supported by Joan and Irwin Jacobs fellowship. N.A. is supported by the Neubauer Family foundation.

Author Contributions

F.E.M. wrote the original draft and performed all the experiments and analysis described in this manuscript except the ones indicated below. E.R.A. helped in setting up the CRISPR-Cas9 screen and proofreading the manuscript. J.K. performed the experiments described in Figure 4a, 4g, and Supplementary Figure 4. A.B. helped in characterizing splicing activity. I.S. helped in analyzing the data related to RBM10 role in DNA replication progression and editing the manuscript. N.A. conceived and supervised the study.

Corresponding Author

Correspondence to Nabieh Ayoub (ayoubn@technion.ac.il).

Competing Interests

The authors declare that they have no competing interest.

Methods

Cell lines and cell culture

HCC827, NCI-H1299, NCI-H1944, and NCI-H1975 cell lines were obtained from ATCC and grown at 37°C and 5% CO2. All cell lines were cultured in RPMI-1640 medium (Gibco) supplemented with 10% heat-inactivated fetal bovine serum (Gibco), 2mM L-glutamine (Gibco), and 100unit/mL penicillin and 100µg/mL streptomycin (Gibco).

Lentiviral transduction

Lentiviral particles were generated by co-transfecting HEK293T cells plated in 10cm plates with 1.64pmol target vector, together with 1.3pmol psPAX2 (Addgene #12260) and 0.72pmol pMD2.G (Addgene #12259) using 3:1 µg PEI to µg DNA ratio. Media containing the viral particles were collected 48 hr post-transfection and filtered with 0.45 µm filters. The indicated cell lines were transduced with the lentiviral particles in the presence of 10µg/ml polybrene (Sigma-Aldrich H9268). At 48 hr post-infection, transduced cells were selected using the appropriate antibiotics.

Generation of flag-Cas9 expressing cells and RBM10 knockout cell lines

To generate HCC827 cell line constitutively expressing Cas9, cells were transduced with Lenti-Cas9-2A-Blast (Addgene #73310) lentiviral particles followed by selection with 10µg/ml blasticidin (Invivogen #ant-bl) for 72 hr. A single clone stably expressing flag-Cas9 fusion was selected and validated by western blot and immunofluorescence. To generate isogenic RBM10 knockout in HCC827 cells expressing flag-Cas9 (HCC827-Cas9), guide RNAs (gRNA) were designed and cloned into pSPgRNA plasmid (Addgene #47108) using BbsI restriction enzyme. HCC827-Cas9 cells were transfected with RBM10 gRNA1 (HCC827-Cas9$^{RBM10\text{-}KO}$ and naïve HCC827$^{RBM10\text{-}KO3}$) or gRNA2 (HCC827-Cas9$^{RBM10\text{-}KO2}$) followed by clonal isolation. Single clones were screened for RBM10 knockout using western blot and validated by immunofluorescence and sequencing. The sequences of RBM10 gRNAs are included in Supplementary Table 1. To generate RBM10 knockout in naïve HCC827 and NCI-H1299 cells, RBM10 gRNA1 was cloned into pSpCas9(BB)-2A-GFP (PX458) (Addgene #48138) and transfected to cells. At 24 hr after transfection, GFP-positive cells were sorted using BD LSRFortessa™ cell analyzer (BD Biosciences) and plated in 96-well plates at a dilution of one cell per well. Single clones were screened for RBM10 knockout using western blot and validated by immunofluorescence and sequencing.

Genome-wide CRISPR-Cas9 synthetic lethal screen

240 million cells of HCC827-Cas9^{WT} and HCC827-Cas9$^{RBM10\text{-}KO}$ were transduced in triplicates with TKOv1 sgRNA library, which contains 91,320 sgRNAs targeting 17,232 protein-coding genes[52], at MOI=0.3 and an average of 500-fold coverage of the library. 24 hr post-transduction, cells were selected with 2 µg/mL puromycin for 2 days. Following selection, 80 × 10^7 cells were harvested as day 0 samples (T0) and the remaining cells were plated and passaged every 5 days for one month. Cells were then collected at day 15 (T15) and day 30 (T30) for isolation of genomic DNA (gDNA) together with the T0 samples. Genomic DNA extraction was performed with Blood & Cell Culture DNA Maxi Kit (Qiagen) according to the manufacturer's instructions. gRNA inserts were amplified using two rounds of PCR reactions. First, a 600bp region of the lentiviral library vectors containing the sgRNA region was amplified using ordinary PCR with Q5 high-fidelity DNA polymerase for 25 cycles. A total of 120µg gDNA was used as template for each sample (60 reactions: 2µg gDNA/50µl reaction). Second, the amplified PCR products were subjected to another PCR reaction with Illumina next-generation sequencing adaptors for 10 cycles and 200bp product was amplified. The resulting amplicons were pooled and gel purified using the NucleoSpin Gel and PCR Clean-up (Macherey-Nagel). Samples were sequenced on a MiSeq platform with ~10 million reads per sample (Illumina). Demultiplexing and mapping of sequencing reads to the gRNA library was performed using Bowtie, allowing 2 mismatches and discarding reads that mapped more than once. Reads were normalized to 10 million reads per sample, excluding gRNAs with less than 10 raw reads in T0 samples. Fold-change for each gRNA was calculated in each replicate versus the T0 sample. Bioinformatic and Bayesian Analysis of Gene Essentiality (BAGEL) algorithm[53] was devised to calculate the essentiality score (Bayes factor – BF) of each gene in parental (WT) and RBM10-KO cells. RBM10 SL genes were defined as genes with BF>5 (i.e. essential) in RBM10-KO cells and BF<2 (i.e. non-essential) in WT cells. Pathway enrichment analysis and gene ontology were conducted using ShinyGO[70].

Conditional short hairpin RNA (shRNA) knockdown

shRNA oligonucleotides directed against the indicated genes were annealed and cloned into Tet-pLKO-puro lentiviral vector (Addgene #21915) digested with *Eco*RI and *Age*I. Lentiviral particles were generated as described above and used to transduce parental and RBM10-KO HCC827-Cas9 cells, followed by selection with 1µg/ml puromycin (Invivogen #ant-pr) for 3 days. Cells were maintained in complete medium in the presence of 0.6µg/ml puromycin. To induce shRNA-mediated gene expression knockdown, cells were cultured in the presence of 0.2µg/ml doxycycline (DOX) for 48 hr prior to clonogenic survival assays. Gene expression

knockdown was validated by RT-qPCR. The shRNA and qPCR primer sequences used in this study are included in Supplementary Table 3.

Generation of RBM10 expression vectors

To generate EGFP-RBM10 expression vectors, RBM10 was amplified from pDest26-RBM10-wt plasmid[41] (gift from Prof. Juan Valcárcel) and cloned into pEGFP-C1 expression plasmid. To generate RBM10-V2, all-round PCR was used to delete RBM10 exon 4. Splicing-mutant RBM10 was generated by site-directed mutagenesis. To constitutively restore RBM10 expression in RBM10-deficient cells, full-length RBM10 was subcloned to Lenti-Cas9-2A-Blast plasmid followed by lentivirus generation and transduction. Primer sequences used for cloning and mutagenesis are included in Supplementary Table 3.

RNA isolation, RT-PCR and qPCR

Total RNA was isolated from cells using the TRIzol reagent according to the manufacturer's instructions (Ambion) and treated with RQ1 DNase (M6101, Promega). 1µg RNA was used for cDNA synthesis using the qScript cDNA Synthesis Kit (Quanta) with random primers. RT-PCR for alternative splicing assay of NUMB and EIF4H genes was performed by standard PCR using Red Load Taq Master (Jena Bioscience) followed by gel electrophoresis in agarose gel stained with ethidium bromide. Band intensities were quantified using GelDoc software. Real-time qPCR for measuring mRNA levels was performed using Step-One-Plus real-time PCR System (Applied Biosystems) and the Fast SYBR Green Master mix (Applied Biosystems) with three technical repeats for each PCR. Data analysis and quantification were performed using StepOne software V2.2 supplied by Applied Biosystems. Primer sequences used for RT-PCR and qPCR are included in Supplementary Table 3.

Small molecule inhibitors and drugs

MK1775 (A5755), Alisertib (MLN8237) (A4110), and hydroxyurea (B2102) were purchased from APExBio.

Immunoblotting

Whole-cell protein extracts were prepared using hot lysis buffer (1%SDS, 5mM EDTA, 50mM Tris, pH7.5) supplemented with protease inhibitor mixture (Calbiochem). Protein samples were diluted and boiled in 5X protein loading buffer (10% SDS, 500mM DTT, 50%Glycerol, 250mM Tris-HCL and 0.5%bromophenol blue dye) and separated on an SDS-polyacrylamide gel. Proteins were transferred to a PVDF membrane (Millipore) and immunoblotted with the indicated antibodies. The following primary antibodies were used for immunoblotting: RBM10 (Sigma-Aldrich cat.no. HPA034972, 1:10,000), FLAG-tag (Sigma-Aldrich cat.no. F7425,

1:4,000), β-actin (Sigma-Aldrich cat.no. A5441, 1:10,000), α-Tubulin (Santa Cruz Bio cat.no. sc-5286, 1:1,000), pRPA32-S4/S8 (Bethyl cat.no. A300-245A, 1:1,000), pRPA32-S33 (Bethyl cat.no. A300-246A, 1:1,000), RPA32 (Abcam cat.no. ab2175, 1:500), γH2AX (Cell Signaling Technology cat.no. 2577, 1:1000), pChk1-S345 (Cell Signaling Technology cat.no. 2348, 1:1,000), Histone H3 (Abcam cat.no. ab1791, 1:30,000), Rad51 (Santa Cruz Bio cat.no. sc-8349, 1:1,000), PARP1 (Enzo Life Sciences cat. no. ALX-210-895, 1:2,000), PCNA (Santa Cruz Bio cat. no. sc-56, 1:1,000), GAPDH (Abcam cat.no. ab8245, 1:1,000), GFP (Santa Cruz Bio cat.no. sc-9996, 1:1,000). The following secondary antibodies were used: anti-rabbit IgG-HRP (Jackson ImmunoResearch cat.no. 111–035-003, 1:20,000), anti-mouse IgG-HRP (Amersham cat.no. NXA931, 1:10,000).

Biochemical fractionation

Cells were lysed with Buffer A for 5 min at 4°C. Cell lysates were centrifuged at 1500× g for 5 min at 4°C and the supernatant (cytoplasmic fraction) was removed. Then, the pellet was incubated with Buffer B (3mM EDTA, 0.2mM EGTA, 1mM DTT, PMSF, and protease inhibitor mixture) for 10 min on ice followed by centrifugation at 1700× g for 5 min at 4°C to extract nuclear-soluble fraction. To prepare chromatin-bound fraction, pellet was resuspended with hot lysis buffer (1%SDS, 5mM EDTA, 50mM Tris, pH7.5), boiled for 15 min, and sonicated with two 15 sec pulses of 35% amplitude, centrifuged at maximum speed for 20 min at 12°C, and the supernatant was recovered. Fractions were subjected to immunoblot analysis with the indicated antibodies.

GFP-trap

HEK293T cells expressing either EGFP only or EGFP-RBM10 plasmids were subjected to GFP-TRAP assay as previously described[71]. Briefly, EGFP-RBM10 expressing cells were treated with DMSO or 300nM MK1775 for 4 hr. Next, cells were lysed in RIPA buffer (150mM NaCl, 50mM Tris pH 7.4, 1% NP40, 0.5% deoxycholate, 0.1% SDS) supplemented with protease inhibitor cocktail and then diluted 1:4 with binding buffer (150mM NaCl, 50mM Tris pH 7.4). 2 milligram of cell lysate was incubated for 4 hr at 4ºC with 15µl GFP-TRAP beads followed by western blot analysis. For GFP-trap followed by mass spectrometry (MS), HEK293T cells were transfected with EGFP-RBM10 and EGFP-RBM10-V2 plasmids, followed by mock or 300nM MK1775 treatment for 4 hr. Cells were lysed and subjected to GFP-trap as described above. Beads were washed 5 times in PBSx1 followed by elution and trypsin digestion. Digested peptides were then analyzed by mass spectrometry (MS) at the Smoler Proteomics Center in the department of Biology in the Technion. The samples were

analyzed by LC-MS/MS using Q-Exactive plus mass spectrometer (Thermo Scientific), coupled to Easy nano LC-1000 capillary UHPLC (Thermo Scientific). Protein identification and intensity analysis was performed using maxquant[72], searching against the human section of the Uniprot database. RBM10-interacting proteins enrichment analysis and gene ontology was conducted using ShinyGO[70].

Immunoprecipitation

For endogenous RBM10 immunoprecipitation, H1299 cells were harvested and lysed in RIPA buffer (150mM NaCl, 50mM Tris pH 7.4, 1% NP40, 0.5% deoxycholate, 0.1% SDS) supplemented with protease inhibitor cocktail. Immunoprecipitations were performed using 0.5µg IgG or RBM10 antibody and protein A magnetic beads (GenScript #L00273) incubated with 2mg lysate overnight at 4ºC. Immunoprecipitated samples were subjected to immunoblot analysis using the indicated antibodies.

Immunofluorescence

Cells were seeded onto glass coverslips and grown for 24 hr followed by drug treatments as indicated in the figure legends. Cells were fixed with 4% (wt/vol) paraformaldehyde for 10 min, permeabilized with 0.5% Triton X-100 in PBS for 10 min, blocked with blocking buffer (4% (wt/vol) BSA, 0.15% Tween 20 and 0.15% Triton X-100 in PBS) for 1 hr at room temperature and incubated with the indicated antibodies for 1 hr at 37°C. Excess antibody was washed three times with wash buffer (0.15% Tween 20 and 0.15% Triton X-100 in PBS × 1), and cells were stained with secondary antibodies for 1 hr at room temperature in the dark, and then washed as above. Coverslips were mounted onto glass slides using VECTASHIELD® Antifade Mounting Medium with DAPI (Vectorlabs). For immunofluorescence staining of γH2AX, pRPA32-S33, and BrdU, cells were pre-extracted with 0.25% Triton X-100 in PBS for 15 min on ice prior to fixation. For EdU incorporation, cells were pulsed with 10µM EdU (5-ethynyl-2-deoxyuridine, Invitrogen A10044) for 30 min at 37ºC, 5% CO2. EdU click reactions were performed after cell permeabilization by incubating cells with EdU staining buffer containing 2mM CuSO4, 100mM ascorbic acid and 1µM AlexaFluor 647 azide (Invitrogen A10277) in PBS for 30 min at room temperature. Images were acquired using inverted Zeiss LSM-700 or LSM-710 confocal microscopes. Image analysis was performed using ImageJ software. The following primary antibodies were used for immunofluorescence: BrdU FITC (BD Biosciences, cat.no. 51-23614 1:1,000), RBM10 (Sigma-Aldrich cat.no. HPA034972, 1:2,000), pRPA32-S33 (Bethyl cat.no. A300-246A, 1:500), γH2AX (Millipore cat.no. 05-636, 1:2,500), FLAG-tag (Sigma-Aldrich cat.no. F7425, 1:1,000), pH3(Ser10) (Cell

Signaling Technology cat.no. 9706, 1:1,000). The following secondary antibodies were used: anti-rabbit IgG Alexa Fluor®488 (Invitrogen cat.no. A-21206, 1:500), anti-mouse IgG Alexa Fluor®488 (Invitrogen cat.no. A-21202, 1:500), anti-rabbit Alexa Fluor®568 (Invitrogen cat.no. A10042, 1:500), anti-mouse Alexa Fluor®568 (Invitrogen cat.no. A10037, 1:500), anti-rabbit Alexa Fluor®647 (Invitrogen cat.no. A-31573, 1:500), anti-mouse IgG Alexa Fluor®647 (Invitrogen cat.no. A32787, 1:500).

Proximity ligation assay (PLA)

Proximity ligation assay (PLA) was performed using the Duolink in situ red starter kit (Sigma-Aldrich) following the manufacturer's instructions. Rabbit anti-RBM10 antibody (Sigma-Aldrich HPA034972, 1:2,000) and mouse anti-PCNA (Santa Cruz Bio cat. no. sc-56, 1:250) antibodies were incubated for 1 hr at 37°C prior to PLA analysis. PLA assay between RBM10 and EdU-labelled nascent DNA was performed as previously described[73]. Briefly, cells were pulse labelled with 100μM EdU for 10 min at 37°C, followed by pre-extraction in 0.25% Triton X-100 in PBS for 10 min on ice and fixation in 4% (wt/vol) paraformaldehyde. Cells were incubated in EdU click reaction buffer containing 2mM CuSO4, 100mM ascorbic acid and 10μM biotin-azide (Invitrogen B10184) in PBS for 1 hr at room temperature. Cells were incubated in blocking buffer for 1 hr at room temperature followed by incubation with rabbit anti-RBM10 (1:2000) and mouse anti-biotin (Jackson ImmunoResearch cat.no. 200-002-211, 1:2000) antibodies for 1 hr at 37°C. Next, PLA assay was performed using the Duolink in situ red starter kit (Sigma-Aldrich) following the manufacturer's instructions. Images were acquired using inverted Zeiss LSM-700 confocal microscope.

Short-term growth delay assay

For determining drug sensitivity, cells were seeded in 96-well plates in duplicates at a density of 2,000-5,000 cells per well. 24 hr post-seeding, drugs were added at the indicated concentrations. Cell viability was measured 72 hr after drug treatment using the CellTiter 96® AQueous One Solution Cell Proliferation Assay (Promega) following the manufacturer's protocol, and absorbance was measured using Epoch Microplate Spectrophotometer (BioTek). Cell viability was normalized to the viability of untreated cells.

Clonogenic survival assays

For colony survival assay, cells seeded onto 6-well plates (500 cells per well) and left untreated or treated with the indicated doses of drugs. After 14 days, cells were fixed in methanol and stained with 0.25% crystal violet. Individual colonies were counted, and relative survival was calculated by normalizing to the number of colonies in control wells.

Annexin-V apoptosis assay

Apoptosis was assessed by annexin V-FITC kit (Invitrogen) according to the manufacturer's instructions. Parental (WT) and RBM10-KO cells were treated with the indicated concentrations of MK1775 for 24 hr prior to analysis. Samples were analyzed using flow cytometry of 10,000 cells on a Cytek Aurora flow cytometer. Results were calculated as the percentage of positive annexin V-FITC cells out of total cells counted.

DNA combing

DNA combing analysis was performed as described[74]. Briefly, unsynchronized cells were pulse labelled with 25uM Idu for 30 min, followed by 600µM CldU for another 30 min, followed by 1.5 hr growth without any label. Cells were harvested into 2% agarose plugs, incubated for 48 hr in a digestion buffer (1% N Laurouylsarcosine, 0.2% Na Deoxycholate, 10mM Tris-HCl pH 7.5, 100mM EDTA, and 1mg/ml proteinase K). Next, TE 50X was added overnight, and the plugs were dissolved into 50mM MES pH6 with 100mM NaCl. The DNA was combed on Genomic vision combing slides, denatured and stained with the following primary antibodies: Rat anti-BrdU (abcam #ab6326, 1:200), mouse anti-BrdU (BD Biosciences #347580, 1:20), and anti-ssDNA antibody (DSHB #AB10805144, 1:20). The following secondary antibodies were used: Goat anti-mouse Alexa Fluor®647 (Jackson Immunoresearch #115-605-166, 1:400), goat anti-rat Alexa Fluor®594 (ThermoFisher Scientific #A11007, 1:400), and anti-mouse IgG2a Alexa Fluor®488 (ThermoFisher Scientific #A21131, 1:500). The slides were photographed with a fluorescent microscope and analyzed using Olympus CellSens program.

Mouse xenograft model

Animal studies and protocols were approved by the Committee on the Ethics of Animal Experiments of the Technion, Israel Institute of Technology (IL-069-07-22). Immunocompromised NOD.CB17-Prkdcscid/NcrCrl (NOD SCID) mice were purchased from Envigo. Mouse model of LUAD cell lines subcutaneous xenografts were established by transplanting cells into 6-week-old female NOD SCID mice. Mice were randomly assigned into control and treatment groups. Prior to initiating any experiments, mice were allowed one week acclimation to housing conditions at the Technion Animal Facility. All mice were housed in a strict pathogen-free environment. 2.5×10^6 of the indicated cells were resuspended in 100µl PBS and mixed 1:1 with Matrigel (High Concentration – Corning) and injected subcutaneously into the right flank of 6 weeks-old female NOD SCID mice. Tumors were measured using digital calipers. Tumor volumes were calculated using the formula: $0.5 \times \text{length} \times \text{width}^2$. When tumors reached ~100mm^3, mice were randomly assigned to treatment groups

(n = 6 mice for each group, unless otherwise indicated). Each group received either control (vehicle), MK1775 (40mg/kg, p.o.), or MK1775 + alisertib (30mg/kg each, p.o.) once daily for 15 days. Mice were euthanized when the tumors of control mice reached ∼1500mm^3 and tumors were excised, weighed, and photographed.

Immunohistochemistry

Tumors excised from mice were fixed in 4% formalin at 4ºC overnight, washed three times with PBS, and immersed in 30% (wt/vol) sucrose solution at 4ºC overnight. Then, tumors were embedded in optimal cutting temperature compound (TissueTek) and frozen at -20ºC and. 10μm cryosections were prepared and permeabilized using 0.5% Triton X-100 in PBS followed by immunofluorescence staining as described above, except primary antibody incubation with γH2AX antibody (Millipore cat.no. 05-636,1:500) were performed at 4ºC overnight.

Data availability

Raw next-generation sequencing data for RBM10 SL CRISPR-Cas9 screen have been deposited in ArrayExpress and are available through accession number E-MTAB-12724. The mass spectrometry proteomics data have been deposited to the ProteomeXchange Consortium via the PRIDE repository with the dataset identifier PXD040109. All data supporting the findings of this study are available from the corresponding author upon request.

References

1. Sung, H. *et al.* Global Cancer Statistics 2020: GLOBOCAN Estimates of Incidence and Mortality Worldwide for 36 Cancers in 185 Countries. *CA Cancer J Clin* **71**, 209–249 (2021).
2. Siegel Mph, R. L. *et al.* Cancer statistics, 2023. *CA Cancer J Clin* **73**, 17–48 (2023).
3. Collisson, E. A. *et al.* Comprehensive molecular profiling of lung adenocarcinoma. *Nature 2014 511:7511* **511**, 543–550 (2014).
4. Vinayanuwattikun, C. *et al.* Elucidating Genomic Characteristics of Lung Cancer Progression from In Situ to Invasive Adenocarcinoma. *Scientific Reports 2016 6:1* **6**, 1–10 (2016).
5. Chen, H. *et al.* Genomic and immune profiling of pre-invasive lung adenocarcinoma. *Nat Commun* (2019) doi:10.1038/s41467-019-13460-3.
6. Wang, Y. *et al.* Distinct gene mutation profiles among multiple and single primary lung adenocarcinoma. *Front Oncol* **12**, 6746 (2022).
7. Seiler, M. *et al.* Somatic Mutational Landscape of Splicing Factor Genes and Their Functional Consequences across 33 Cancer Types. *Cell Rep* (2018) doi:10.1016/j.celrep.2018.01.088.
8. Rao, W. *et al.* Frequently mutated genes in predicting the relapse of stage I lung adenocarcinoma. *Clin Transl Oncol* (2023) doi:10.1007/S12094-023-03074-Z.
9. Cao, Y. *et al.* RNA-binding motif protein 10 represses tumor progression through the Wnt/β- catenin pathway in lung adenocarcinoma. *Int J Biol Sci* **18**, 124–139 (2022).

10. Hernández, J. *et al.* Tumor suppressor properties of the splicing regulatory factor RBM10. *RNA Biol* **13**, 466–472 (2016).
11. Zhang, S. *et al.* RNA binding motif protein 10 suppresses lung cancer progression by controlling alternative splicing of eukaryotic translation initiation factor 4H. *EBioMedicine* **61**, 103067 (2020).
12. Zhao, J. *et al.* Functional analysis reveals that RBM10 mutations contribute to lung adenocarcinoma pathogenesis by deregulating splicing. *Sci Rep* **7**, (2017).
13. Nanjo, S. *et al.* Deficiency of the splicing factor RBM10 limits EGFR inhibitor response in EGFR-mutant lung cancer. *J Clin Invest* **132**, (2022).
14. Zappa, C. & Mousa, S. A. Non-small cell lung cancer: current treatment and future advances. *Transl Lung Cancer Res* **5**, 288 (2016).
15. Herbst, R. S., Morgensztern, D. & Boshoff, C. The biology and management of non-small cell lung cancer. *Nature 2018 553:7689* **553**, 446–454 (2018).
16. Xie, M., Xu, X. & Fan, Y. KRAS-Mutant Non-Small Cell Lung Cancer: An Emerging Promisingly Treatable Subgroup. *Front Oncol* **11**, 1535 (2021).
17. Cooper, A. J., Sequist, L. v. & Lin, J. J. Third-generation EGFR and ALK inhibitors: mechanisms of resistance and management. *Nature Reviews Clinical Oncology 2022 19:8* **19**, 499–514 (2022).
18. Pio, R. & Montuenga, L. M. Alternative splicing in lung cancer. *J Thorac Oncol* **4**, 674–678 (2009).
19. Bonnal, S. C., López-Oreja, I. & Valcárcel, J. Roles and mechanisms of alternative splicing in cancer — implications for care. *Nature Reviews Clinical Oncology 2020 17:8* **17**, 457–474 (2020).
20. Zhao, J. *et al.* Systematic profiling of alternative splicing signature reveals prognostic predictor for prostate cancer. *Cancer Sci* **111**, 3020–3031 (2020).
21. Coomer, A. O., Black, F., Greystoke, A., Munkley, J. & Elliott, D. J. Alternative splicing in lung cancer. *Biochim Biophys Acta Gene Regul Mech* **1862**, (2019).
22. de Fraipont, F., Gazzeri, S., Cho, W. C. & Eymin, B. Circular RNAs and RNA splice variants as biomarkers for prognosis and therapeutic response in the liquid biopsies of lung cancer patients. *Front Genet* **10**, (2019).
23. Cherry, S. & Lynch, K. W. Alternative splicing and cancer: insights, opportunities, and challenges from an expanding view of the transcriptome. *Genes Dev* **34**, 1005–1016 (2020).
24. Li, Z. *et al.* The RNA-Binding Motif Protein Family in Cancer: Friend or Foe? *Front Oncol* **11**, (2021).
25. Stanley, R. F. & Abdel-Wahab, O. Dysregulation and therapeutic targeting of RNA splicing in cancer. *Nat Cancer* **3**, 536–546 (2022).
26. Machour, F. E. *et al.* RBM6 splicing factor promotes homologous recombination repair of double-strand breaks and modulates sensitivity to chemotherapeutic drugs. *Nucleic Acids Res* **49**, 11708–11727 (2021).
27. Inoue, A., Takahashi, K. P., Kimura, M., Watanabe, T. & Morisawa, S. Molecular cloning of a RNA binding protein, S1-1. *Nucleic Acids Res* **24**, 2990–2997 (1996).
28. Owczarek-Lipska, M., Markus, F., Bültmann, E., Korenke, G. C. & Neidhardt, J. A TARP Syndrome Phenotype Is Associated with a Novel Splicing Variant in RBM10. *Genes (Basel)* **13**, (2022).
29. Daicheng, H., Shiwen, X., Jingxuan, Z., Junbo, H. & Bo, W. A Frameshift RBM10 Variant Associated With TARP Syndrome. *Front Genet* **13**, (2022).
30. Gebauer, F., Schwarzl, T., Valcárcel, J. & Hentze, M. W. RNA-binding proteins in human genetic disease. *Nat Rev Genet* **22**, 185–198 (2021).

31. Højland, A. T. *et al.* First reported adult patient with TARP syndrome: A case report. *Am J Med Genet A* **176**, 2915 (2018).
32. Imagawa, E., Konuma, T., Cork, E. E., Diaz, G. A. & Oishi, K. A novel missense variant in RBM10 can cause a mild form of TARP syndrome with developmental delay and dysmorphic features. *Clin Genet* **98**, 606–612 (2020).
33. Gripp, K. W. *et al.* Long-term survival in TARP syndrome and confirmation of RBM10 as the disease-causing gene. *Am J Med Genet A* **155**, 2516–2520 (2011).
34. Johnston, J. J. *et al.* Massively parallel sequencing of exons on the X chromosome identifies RBM10 as the gene that causes a syndromic form of cleft palate. *Am J Hum Genet* **86**, 743–748 (2010).
35. Wang, Y. *et al.* Integrative analysis revealed the molecular mechanism underlying RBM10-mediated splicing regulation. *EMBO Mol Med* **5**, 1431–1442 (2013).
36. Loiselle, J. J. & Sutherland, L. C. RBM10: Harmful or helpful-many factors to consider. *J Cell Biochem* **119**, 3809–3818 (2018).
37. Rodor, J., FitzPatrick, D. R., Eyras, E. & Cáceres, J. F. The RNA-binding landscape of RBM10 and its role in alternative splicing regulation in models of mouse early development. *RNA Biol* **14**, 45–57 (2017).
38. Dou, X. Q. *et al.* Alternative splicing of VEGFA is regulated by RBM10 in endometrial cancer. *Kaohsiung J Med Sci* **36**, 13–19 (2020).
39. Inoue, A. *et al.* RBM10 regulates alternative splicing. *FEBS Lett* **588**, 942–947 (2014).
40. Sutherland, L. C. *et al.* Splicing arrays reveal novel RBM10 targets, including SMN2 pre-mRNA. *BMC Mol Biol* **18**, 1–14 (2017).
41. Bechara, E. G., Sebestyén, E., Bernardis, I., Eyras, E. & Valcárcel, J. RBM5, 6, and 10 differentially regulate NUMB alternative splicing to control cancer cell proliferation. *Mol Cell* **52**, 720–733 (2013).
42. Yamada, H. *et al.* Src Family Tyrosine Kinase Signaling Regulates FilGAP through Association with RBM10. *PLoS One* **11**, (2016).
43. Mohan, N., Kumar, V., Kandala, D. T., Kartha, C. C. & Laishram, R. S. A Splicing-Independent Function of RBM10 Controls Specific 3' UTR Processing to Regulate Cardiac Hypertrophy. *Cell Rep* **24**, 3539–3553 (2018).
44. Kunimoto, H. *et al.* RBM10 regulates centriole duplication in HepG2 cells by ectopically assembling PLK4-STIL complexes in the nucleus. *Genes Cells* **25**, 100–110 (2020).
45. Weigt, M. *et al.* Rbm10 facilitates heterochromatin assembly via the Clr6 HDAC complex. *Epigenetics Chromatin* **14**, (2021).
46. Inoue, A. RBM10: Structure, functions, and associated diseases. *Gene* **783**, (2021).
47. Atsumi, T. *et al.* Rbm10 regulates inflammation development via alternative splicing of Dnmt3b. *Int Immunol* **29**, 581–591 (2017).
48. Xiao, W. *et al.* RBM10 regulates human TERT gene splicing and inhibits pancreatic cancer progression. *Am J Cancer Res* **11**, 157 (2021).
49. Cao, Y. *et al.* RBM10 recruits METTL3 to induce N6-methyladenosine-MALAT1-dependent modification, inhibiting the invasion and migration of NSCLC. *Life Sci* **315**, (2023).
50. Jin, X. *et al.* RBM10 inhibits cell proliferation of lung adenocarcinoma via RAP1/AKT/CREB signalling pathway. *J Cell Mol Med* **23**, 3897–3904 (2019).
51. Jung, J. H. *et al.* RNA-binding motif protein 10 induces apoptosis and suppresses proliferation by activating p53. *Oncogene* **39**, 1031–1040 (2020).
52. Hart, T. *et al.* High-Resolution CRISPR Screens Reveal Fitness Genes and Genotype-Specific Cancer Liabilities. *Cell* (2015) doi:10.1016/j.cell.2015.11.015.

53. Hart, T. & Moffat, J. BAGEL: a computational framework for identifying essential genes from pooled library screens. *BMC Bioinformatics* **17**, (2016).
54. Ghelli Luserna Di Rorà, A., Cerchione, C., Martinelli, G. & Simonetti, G. A WEE1 family business: regulation of mitosis, cancer progression, and therapeutic target. *J Hematol Oncol* **13**, (2020).
55. Elbæk, C. R., Petrosius, V. & Sørensen, C. S. WEE1 kinase limits CDK activities to safeguard DNA replication and mitotic entry. *Mutation Research/Fundamental and Molecular Mechanisms of Mutagenesis* **819–820**, 111694 (2020).
56. Bukhari, A. B., Chan, G. K. & Gamper, A. M. Targeting the DNA Damage Response for Cancer Therapy by Inhibiting the Kinase Wee1. *Front Oncol* **12**, 347 (2022).
57. da Costa, A. A. B. A., Chowdhury, D., Shapiro, G. I., D'Andrea, A. D. & Konstantinopoulos, P. A. Targeting replication stress in cancer therapy. *Nat Rev Drug Discov* **22**, 38–58 (2023).
58. Hirai, H. *et al.* Small-molecule inhibition of Wee1 kinase by MK-1775 selectively sensitizes p53-deficient tumor cells to DNA-damaging agents. *Mol Cancer Ther* **8**, 2992–3000 (2009).
59. Weinstein, J. N. *et al.* The Cancer Genome Atlas Pan-Cancer analysis project. *Nat Genet* **45**, 1113–1120 (2013).
60. Kavanaugh, G. *et al.* A whole genome RNAi screen identifies replication stress response genes. *DNA Repair (Amst)* **35**, 55–62 (2015).
61. Kong, A. & Mehanna, H. WEE1 Inhibitor: Clinical Development. *Curr Oncol Rep* **23**, (2021).
62. Lee, J. W. *et al.* Combined Aurora Kinase A (AURKA) and WEE1 Inhibition Demonstrates Synergistic Antitumor Effect in Squamous Cell Carcinoma of the Head and Neck. *Clin Cancer Res* **25**, 3430–3442 (2019).
63. Coulombe, P. *et al.* The ORC ubiquitin ligase OBI1 promotes DNA replication origin firing. *Nature Communications 2019 10:1* **10**, 1–14 (2019).
64. Zheng, H., Shao, F., Martin, S., Xu, X. & Deng, C. X. WEE1 inhibition targets cell cycle checkpoints for triple negative breast cancers to overcome cisplatin resistance. *Sci Rep* **7**, (2017).
65. Chen, D. *et al.* Wee1 Inhibitor AZD1775 Combined with Cisplatin Potentiates Anticancer Activity against Gastric Cancer by Increasing DNA Damage and Cell Apoptosis. *Biomed Res Int* **2018**, (2018).
66. Aarts, M. *et al.* Forced mitotic entry of S-phase cells as a therapeutic strategy induced by inhibition of WEE1. *Cancer Discov* **2**, 524–539 (2012).
67. Rajeshkumar, N. V. *et al.* MK-1775, a potent Wee1 inhibitor, synergizes with gemcitabine to achieve tumor regressions, selectively in p53-deficient pancreatic cancer xenografts. *Clin Cancer Res* **17**, 2799–2806 (2011).
68. Awwad, S. W., Serrano-Benitez, A., Thomas, J. C., Gupta, V. & Jackson, S. P. Revolutionizing DNA repair research and cancer therapy with CRISPR-Cas screens. *Nat Rev Mol Cell Biol* (2023) doi:10.1038/S41580-022-00571-X.
69. Gallo, D. *et al.* CCNE1 amplification is synthetic lethal with PKMYT1 kinase inhibition. *Nature 2022 604:7907* **604**, 749–756 (2022).
70. Ge, S. X., Jung, D., Jung, D. & Yao, R. ShinyGO: a graphical gene-set enrichment tool for animals and plants. *Bioinformatics* **36**, 2628–2629 (2020).
71. Khoury-Haddad, H. *et al.* PARP1-dependent recruitment of KDM4D histone demethylase to DNA damage sites promotes double-strand break repair. *Proc Natl Acad Sci U S A* **111**, (2014).

72. Cox, J. & Mann, M. MaxQuant enables high peptide identification rates, individualized p.p.b.-range mass accuracies and proteome-wide protein quantification. *Nature Biotechnology 2008 26:12* **26**, 1367–1372 (2008).
73. Roy, S., Luzwick, J. W. & Schlacher, K. SIRF: Quantitative in situ analysis of protein interactions at DNA replication forks. *Journal of Cell Biology* **217**, 1521–1536 (2018).
74. Kaykov, A., Taillefumier, T., Bensimon, A. & Nurse, P. Molecular Combing of Single DNA Molecules on the 10 Megabase Scale. *Scientific Reports 2016 6:1* **6**, 1–9 (2016).